International Journal of Heat and Mass Transfer 52 (2009) 4435–4448

Contents lists available at ScienceDirect

International Journal of Heat and Mass Transfer

journal homepage: www.elsevier.com/locate/ijhmt

# Experimental study on the heat transfer under impinging elliptic jet array along a film hole surface using liquid crystal thermograph

Han-Chieh Chiu [a], Jer-Huan Jang [b], Wei-Mon Yan [c,*]

[a] Department of Mechanical Engineering, Technology and Science Institute of Northern Taiwan, Pei-To, Taipei 112, Taiwan, ROC
[b] Department of Mechanical Engineering, Ming Chi University of Technology, Tai-Shan, Taipei 243, Taiwan, ROC
[c] Department of Mechatronic Engineering, Huafan University, Shih Ting, Taipei 223, Taiwan, ROC

ARTICLE INFO

*Article history:*
Received 18 September 2008
Received in revised form 18 March 2009
Accepted 18 March 2009
Available online 13 May 2009

*Keywords:*
Impinging elliptic jet array
Film hole
Liquid crystal thermograph
Aspect ratio

ABSTRACT

In this research, the effects of jet geometry and the arrangement of film holes on the target plate on the impinging heat transfer are experimentally investigated in detail. A liquid crystal thermograph technology is employed in this study. The aspect ratios (AR) of elliptical jet with five different values, 4, 2, 1, 0.5, and 0.25, jet Reynolds number ranging from 2000 to 4000, and jet-to-target spacing ranging from 1.5 to 4.5 are considered to investigate impingement heat transfer performance. In addition, three arrangements of film hole on the target plates, named side-, middle- and staggered-types, are tested, respectively. The experimental results show that the *Nu* increases with the increase of jet Reynolds number. Better heat transfer is noted for the cases with smaller jet-to-plate spacing. For the effect of the arrangement of pores on the target surface, the heat transfer on middle-type plate is more significant than the other two for smaller jet-to-plate spacing. As for the effect of aspect ratio, results indicate that the optimal heat transfer performance is found with circular jet of AR = 1.



## 1. Introduction

Enhancement of heat transfer between fluid and a solid surface is always an important issue in engineering applications, such as thermal management of microelectronic components, compact heat exchangers, gas turbine cooling and the tempering and annealing of glass, etc. Due to the high local heat transfer coefficient, jet impingement is one of the effective methods of heat transfer enhancement in a variety of applications. A survey of configurations used in jet impingement heat transfer studies is available in Viskanta [1]. Many studies have been performed to investigate the jet impingement heat transfer characteristics through experiments and numerical calculations [1,2]. Obot et al. [3] reported that the nozzle exit configuration is the most important factor affecting the heat transfer near the stagnation region. Kataoka [4] investigated the role of artificially induced large-scale eddies on the impingement heat transfer. Among these studies, heat transfer enhancement with a single rectangular or round jet impinging on the surface was investigated most extensively. Tam and Norum [5] studied supersonic rectangular impinging jets from the acoustics point of view. Concerning the effect of jet geometry, elliptic jets are quite different from the extensively studied plane and circular jets mainly due to the fact that the azimuthal curvature variation of a vortical structure causes its non-uniform self-induction. Hussain and Husain [6–8] investigated elliptical jets of different aspect ratios and initial conditions, and effects of excitations at selected frequencies and amplitudes. Ho and Gutmark [9] discussed the mass entrainment and its mechanism in an elliptic jet. Lee and his colleagues [10,11] investigated the local heat transfer characteristics of an elliptic impingement jet. The elliptic jet has general flow characteristics of axisymmetric jets and plane jets. But the flow characteristics of the elliptic jet having large entrainment and strong mixing are quite different from those of axisymmetric or plant jets.

For the heat transfer associated with an array of impinging jets, the effects of the of jet array pattern [12], Reynolds number, cross-flow [13,14], jet-to-target distance [10] and their coupling effects significantly influence the flow and heat transfer characteristics. There have been a number of attempts to complement jet impingement with other enhancing techniques such as cross-flow and ribs [15,16]. Attempts have been made to optimize each method in order to obtain effective heat transfer with low pressure loss. Treuren et al. [17], Rhee et al. [18], Kanokjaruvijit and Martinez-botas [19] and Huang and his colleagues [20,21] investigated detailed heat transfer distributions under arrays of jet impinging on a target plate with dimpled or film hole surfaces. However, their studies only focused on the heat transfer under in-line arrays of jet impinging on a surface. Wagner et al. [22] showed curvature effects have an influence on the obtained results from investigations on a hollow cylinder model. Extended surfaces enhance convective heat transfer in many applications through both an increase in the

* Corresponding author.
*E-mail address:* wmyan@cc.hfu.edu.tw (W.-M. Yan).

0017-9310/$ - see front matter © 2009 Elsevier Ltd. All rights reserved.
doi:10.1016/j.ijheatmasstransfer.2009.03.054

**Nomenclature**

| | |
|---|---|
| AR | aspect ratio of elliptic jet hole |
| $d$ | equivalent diameter of impinging elliptic jet port |
| $h$ | local heat transfer coefficient, W/m$^2$ K |
| $k$ | thermal conductivity of acrylic material, W/m K |
| $k_f$ | air thermal conductivity, W/m K |
| $Nu$ | Nusselt number, $hd/k_f$ |
| $Re$ | jet Reynolds number, $Vd/v$ |
| $T_i$ | initial temperature of the target surface, °C or K |
| $T_\infty$ | mainstream temperature of the air flow, °C or K |
| $T_w$ | color change temperature of the liquid crystal, red-to-green, °C or K |
| $t$ | transient test time, s |
| $V$ | average velocity of impinging jet, m/s |
| $X, x$ | dimensionless and dimensional axial distance of the target surface, $X = x/d$ |
| $Y, y$ | dimensionless and dimensional spanwise distance, $Y = y/d$ |
| $Z, z$ | dimensionless and dimensional spacing between jet plate and target plate, $Z = z/d$ |

*Greek symbols*

| | |
|---|---|
| $\alpha$ | thermal diffusivity of acrylic material, m$^2$/s |
| $\gamma$ | dimensionless time variable defined in Eq. (2), $h\sqrt{\alpha t}/k$ |
| $v$ | kinematic viscosity of air, m$^2$/s |
| $\tau_j$ | time step, s |

convective surface area and the modification of the heat transfer coefficient due to the increased flow turbulence [23–25]. Gau and Chung [26] studied the surface curvature effects on the different size of slot-air-jet impingement cooling flow structure and heat transfer around a concave/convex side of a heated semicylindrical surface. Rhee et al. [18] describe heat transfer, mass transfer, and flow characteristics from arrays of effusion holes Miao and Wu [27] numerically studied the effects of blowing ratio and hole's shape on the distributions of flow field and adiabatic film cooling effectiveness over a flat plate collocated with two rows of injection holes in staggered-hole arrangement.

Thermochromic liquid crystal (TLC) has been widely used as a reliable temperature sensor in the impinging jet heat transfer studies [28,29]. Yan et al. [30] have studied the heat transfer of a flat plate under various jet geometry and air flow velocity. In that study, the optimal performance appeared at different aspect ratio depending on Reynolds number. Usually for data reduction purposes, the assumption of a flat surface has been made. As mentioned earlier, most studies concentrated on jets impinging on smooth, flat surfaces. However, the surface which needs to be cooled may not be smooth for a practical situation. The new studies of jet impingement combined with roughened surfaces have generally promising results [31]. Chyu et al. [32] examined heat transfer performance of multiple delta wings using a transient liquid crystal technique. Hwang and Cheng [33] experimentally studied the local heat transfer coefficients and static wall pressure drops in leading-edge triangular ducts cooled by wall/impinged jets by using transient liquid crystal technique.

In engineering applications, drilling holes is easier than putting barriers on the cooling surface. From the literatures cited from above, it is found that the effects of jet geometry on the impinging heat transfer along film hole surfaces are not well examined. Array design of film holes on a cooling surface has not been studied extensively. The main objective of this study is to investigate the

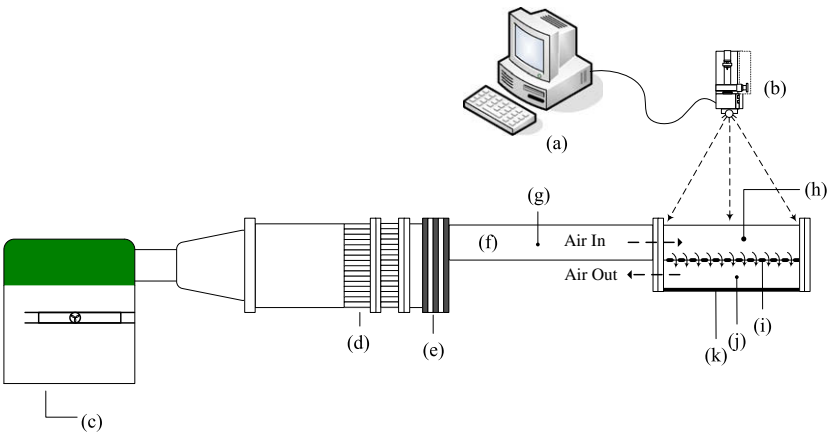


(a) PC+Frame Grabber (b) color camcorder
(c) hot stream generator (d) honeycomb
(e) settling chamber (f) channel
(g) thermocouple (h) pressure chamber
(i) impinging jet orifice plate (j) impinging chamber
(k) impinging target surface coated with thermal liquid crystal

**Fig. 1.** Schematic diagram of the experimental facility.

detailed heat transfer coefficient distributions over a film hole surface under impingement of in-line elliptic jet arrays using a transient liquid crystal technique. This technique had been used to study the heat transfer of plane surface with jet array [30]. In that study, the optimal performance appeared at different aspect ratio depending on Reynolds number. Based on the technique of [30], plates with different film hole arrangement are explored to see the heat transfer augmentation.

## 2. Experimental facility and procedure

Fig. 1 shows a schematic of the whole experimental facility. It consists of a hot steam generator, a honeycomb set, a settling chamber, a channel, a computerized data acquisition module, an image process system and a test section which contains liquid crystal. There is a blower and electrical heater inside the hot steam generator. The channel contains a test section of square cross-section, 100 mm × 100 mm in cross-section area and 300 mm in length, through which the flow develops before entering to the pressure chamber. Hot stream comes from the blower (65 mm in diameter), flows through a 200 mm long expansion section, a 150 mm long settling chamber, an aluminum honey comb (60 mm in length), a 50 mm long buffer zone, and five layers of meshes, and finally enters the test section. The average jet velocity through each jet hole is measured by using a Pitot-tube.

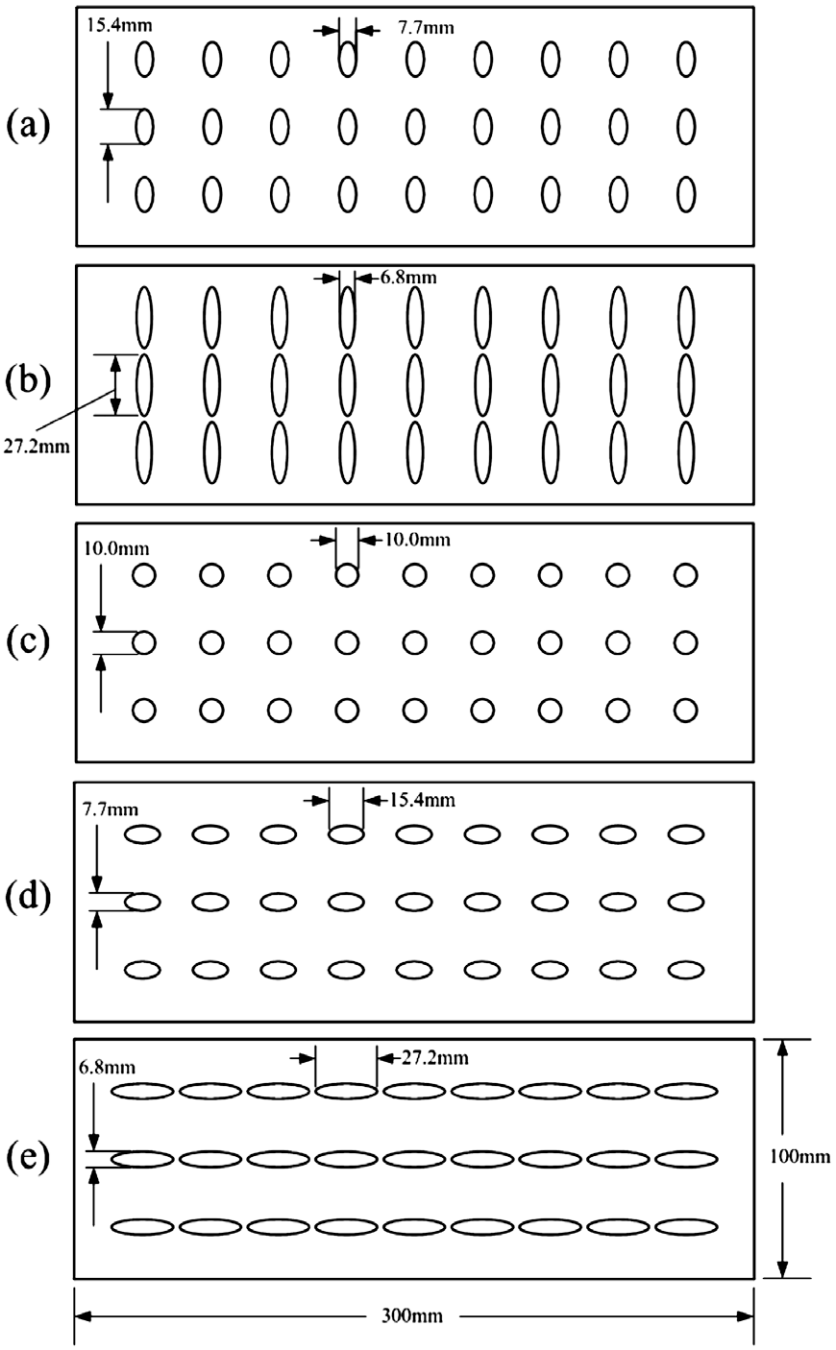


**Fig. 2.** The orifice array with different AR (a) 0.5; (b) 0.25; (c) 1; (d) 2; and (e) 4.

The test section is made of clear acrylic material so that the camera can see through. It consists of two chambers, pressure chamber and impingement chamber, separated by a jet orifice plate. This plate contains an array of elliptic orifices and allows air to flow through. The hot air enters the upper (pressure) chamber to form fully developed flow. This stream then flows through the elliptic holes and impinges onto the target plate which is placed on the bottom of the impingement chamber. There are 9(streamwise) × 3(spanwise) jet elliptic holes arranged in an in-line pattern on the jet plate. The center-to-center distance between two neighboring jet holes are 3d in both the streamwise and spanwise directions, respectively. Different aspect ratios of elliptic orifices are used to investigate the effects on heat transfer. The aspect ratio AR, defined as the ratio of radii in longitudinal and transverse directions of channel, is set 0.25, 0.5, 1.0, 2.0, and 4.0 as shown in Fig. 2. On the target plate, there are film holes. The arrangements of film holes are of side, middle, and staggered types as shown in Fig. 3. Both orifice plate and the target plate have the dimension of 300 mm × 100 mm (length × width). They are 5 mm and 8 mm in thickness, respectively. Thermal liquid crystal SPN/R38C5 W, produced by Hallcrest, is sprayed uniformly on the top surface of the target plate. The temperature distribution of the tar-

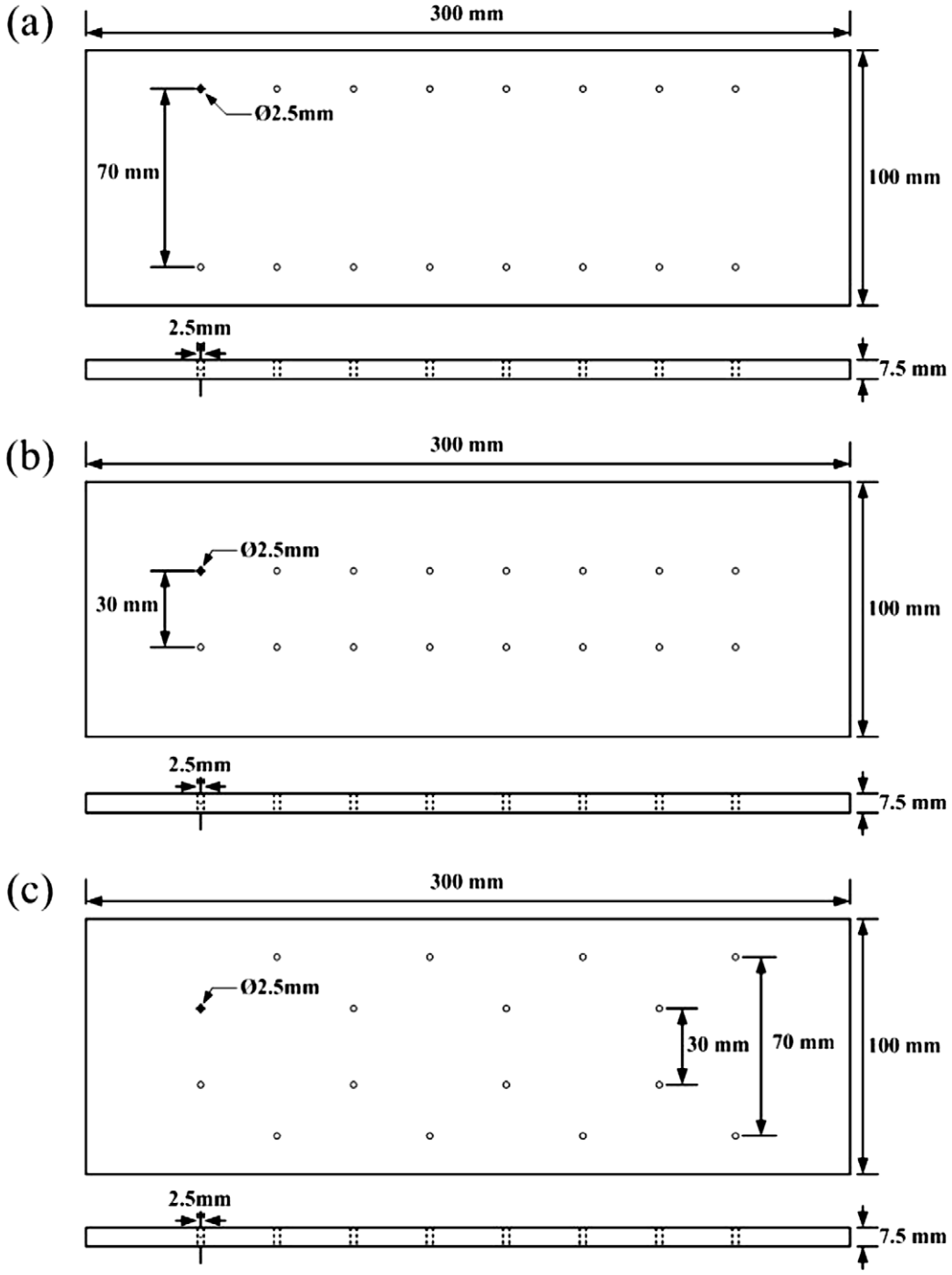


**Fig. 3.** The arrangement of the film holes: (a) side-type; (b) middle-type; and (c) staggered-type.

get plate surface can be shown through the colored image of the liquid crystal. The measurable temperature of the liquid crystal ranges between 33 °C and 43 °C with the middle temperature of 38 °C corresponding to green color. To achieve the most effective conditions, based on the results of [30], air flow is designed to enter the pressure chamber from left ($X = 0$) and to exit at both ends ($X = 0$ and 30) of the impingement chamber. In addition, three conditions of velocities corresponding to Reynolds number of 2000, 3000, and 4000, respectively, are set during the experiment by adjusting the flow rate.

The image processing system used in this work is composed of a digital color camcoder JVC DV (GR-D370TW) and a LCIA image analysis software. The digital camcorder was set over the test section to get the thermal image of the thermal liquid crystal. The isotherms of red-to-blue transition band were captured through the digital color camcorder and were analyzed with LCIA. The recorded data were further processed to obtain non-dimensional results, presented as Nusselt number distributions. A temperature calibration was carried on to avoid the error due to thickness of liquid crystal, angle of camcorder, and light illuminator, etc. The TLC and thermocouples with a FLUKE Helios Plus data logger were used. The measurements of the flow field and the outflow velocity from the jet array are done with equipment Testo 400. The jet Reynolds number is also calculated. The liquid crystal was calibrated using the digital image processing system under the same conditions of experimental runs, including the illuminating light and the camera-viewing angle under the conditions of the laboratory. In this work, the green color appears at 39.2 °C. During each test run, the air mass flow rate was set for the required Reynolds number. The air is heated by an electric heater in the blower section. At the exit of the heater, the air temperature is set based on the experience of test runs to produce acceptable time period for color-change response. More detailed experimental procedure is available elsewhere [16,30].

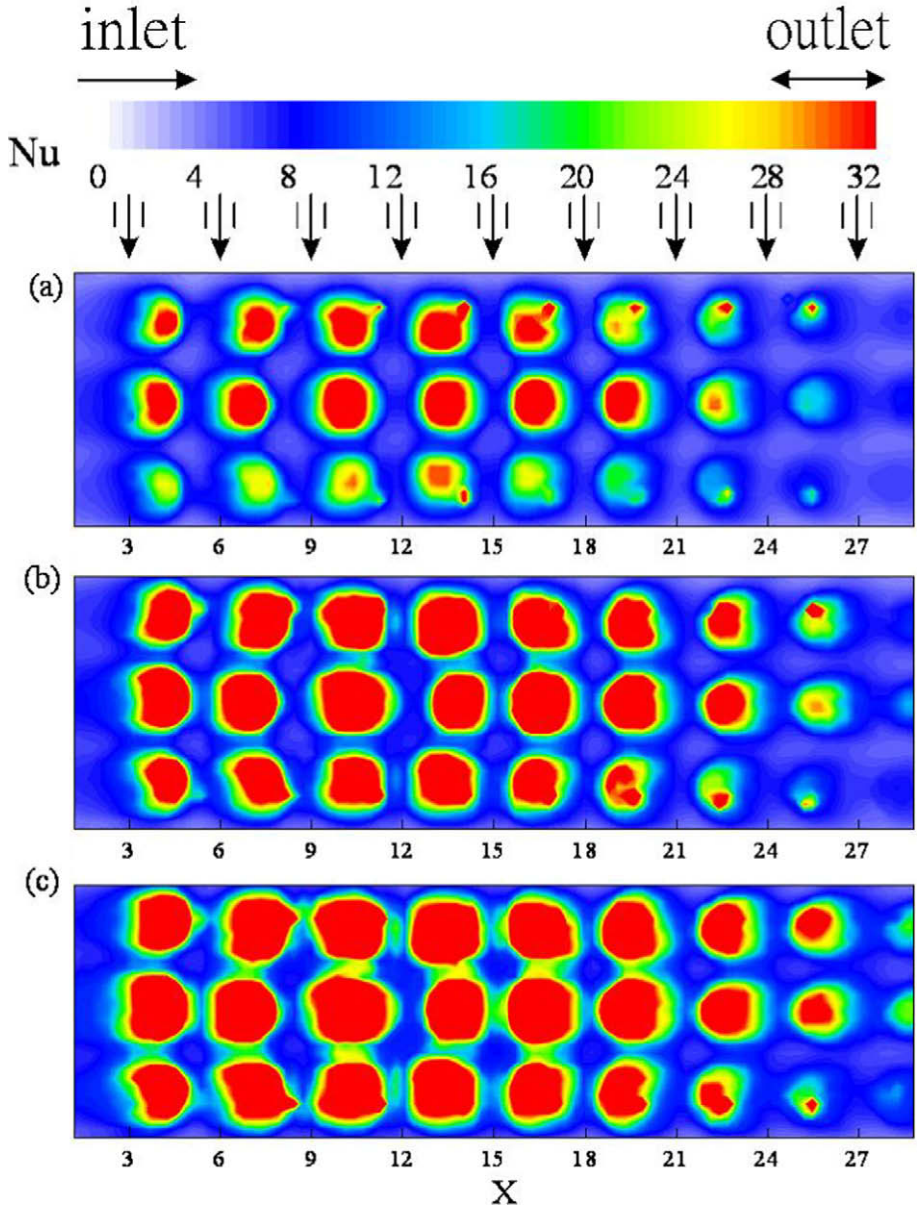


**Fig. 4.** The effects of Reynolds number on the distributions of Nusselt number for side-type target plate with *Re* of (a) 2000; (b) 3000; and (c) 4000.

## 3. Theoretical modeling

During a test period, the heat penetrating depth into the plate is less than the thickness of the target plate for the acrylic plastic test surface material used. Besides, the lateral conduction in the plate is considered insignificant for the local surface temperature response. Hence the local surface temperature on the target plate is thus represented by the classical one-dimensional response of a semi-infinite medium to the sudden step application of a fluid flow at temperature $T_\infty$. The surface temperature can be expressed as

$$(T_w - T_i)/(T_\infty - T_i) = 1 - \exp(\gamma^2)\mathrm{erfc}(\gamma) \quad (1)$$

where

$$\gamma = h\sqrt{\alpha t}/k \quad (2)$$

In the above, $T_i$ represents the initial temperature of the test surface and the $T_\infty$ stands for the jet flow temperature. The thermal diffusivity $\alpha$ and the thermal conductivity $k$ of the Acrylic material are known. To determine the local heat transfer coefficient $h$ on the target surface, the temperature $T_w$ for the color of the coated-surface turning into green was determined according to the calibration test of temperature change of the liquid crystal. The corresponding time, $t$, to reach the temperature for any surface is measured by using the image processing system. The time required for color change in a typical test run is about 15–90 s depending on the experimental conditions as well as the measurement locations.

In the present experimental runs, the target surface will not actually subjected to a step change in the driving air temperature due to the transient heating of the upstream jet plate and duct walls. Nevertheless, Eq. (1) is a fundamental solution that can be used to represent the response to a superposed set of gradual

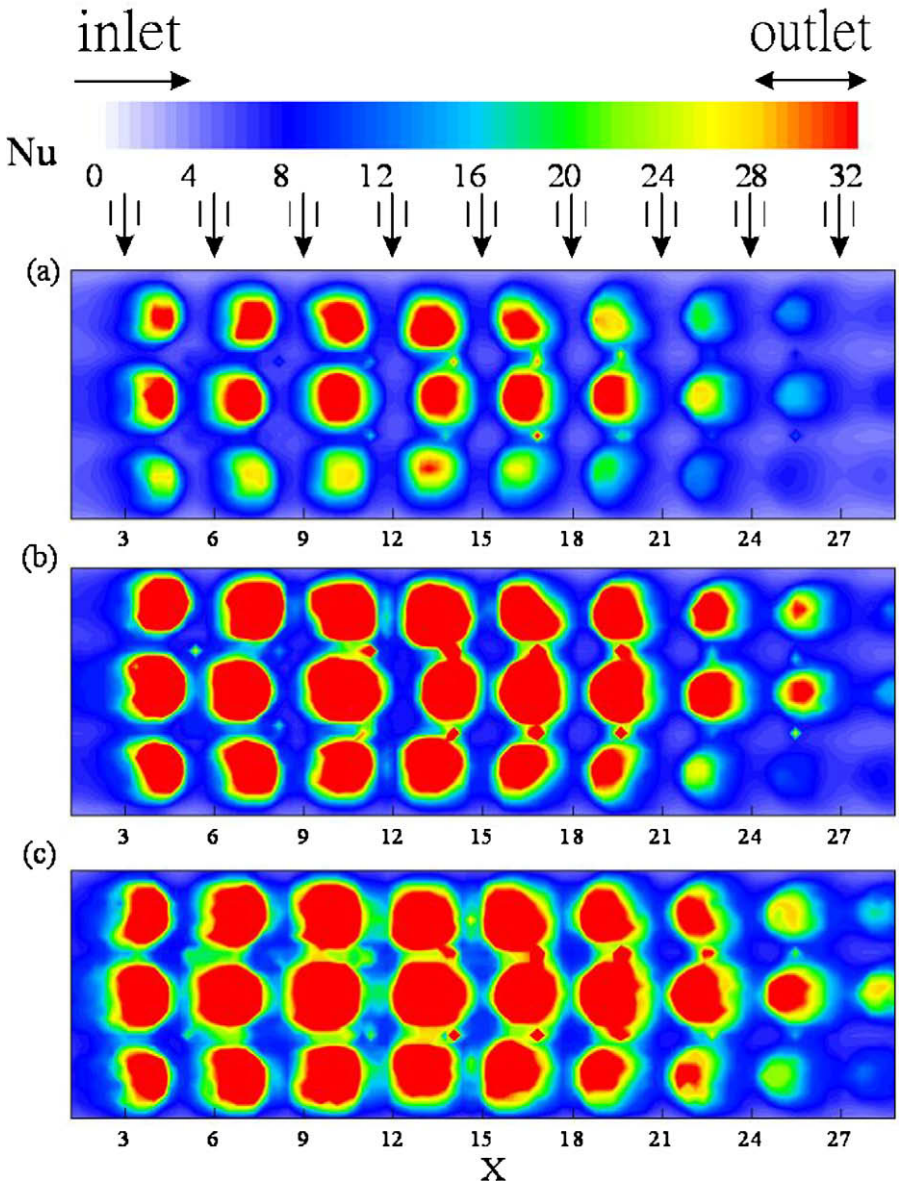


**Fig. 5.** The effects of Reynolds number on the distributions of Nusselt number for middle-type target plate with *Re* of (a) 2000; (b) 3000; and (c) 4000.

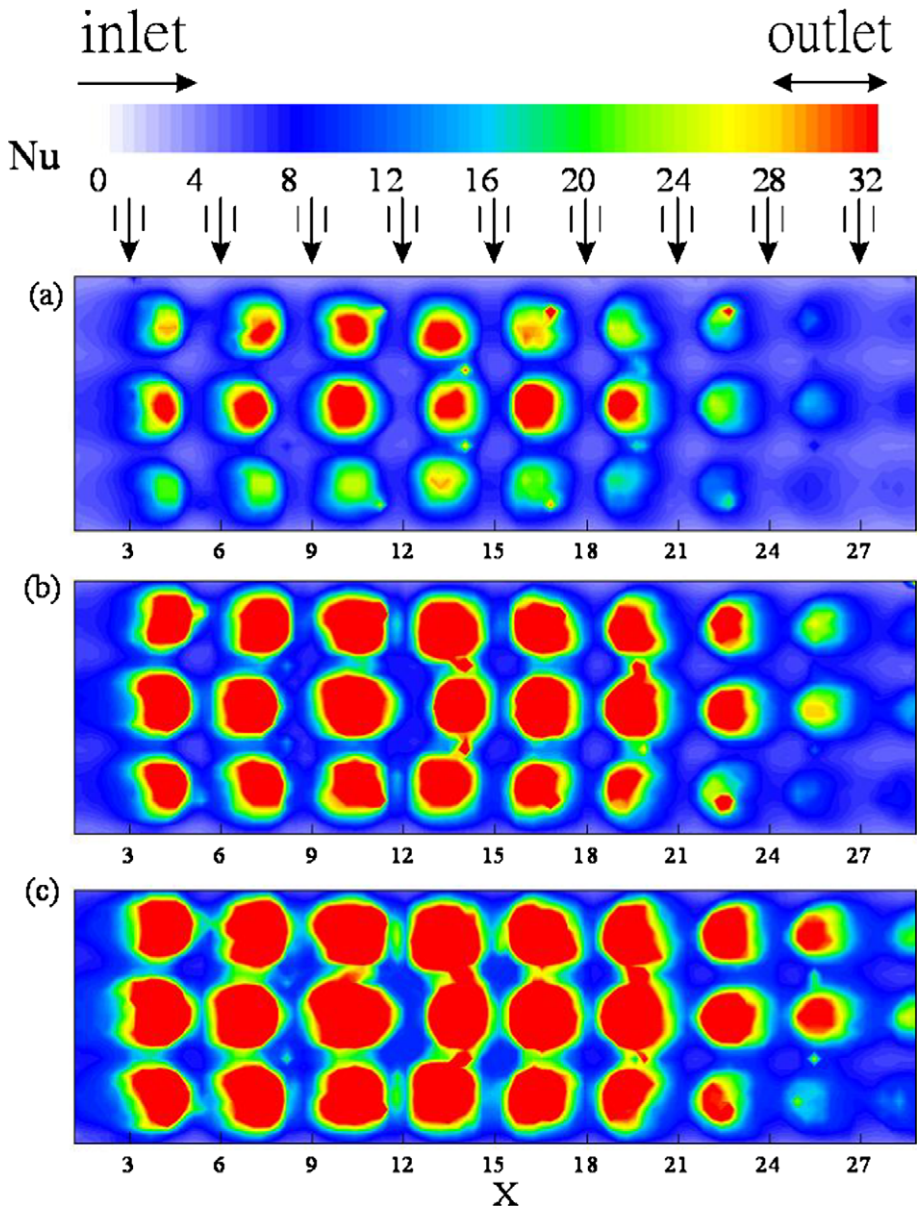


**Fig. 6.** The effects of Reynolds number on the distributions of Nusselt number for staggered-type target plate with *Re* of (a) 2000; (b) 3000; and (c) 4000.

changes in $T_\infty$. Using Duhamel's superposition theorem, the solution in Eq. (1) can be expressed as

$$T_w - T_i = \sum_{j=1}^{n} \left\{ 1 - \exp\left[\frac{h^2\alpha(t-\tau_j)}{k^2}\right] \operatorname{erfc}\left[\frac{h\sqrt{\alpha(t-\tau_j)}}{k}\right] \right\} [\Delta T_{\infty j}] \qquad (3)$$

where $\Delta T_\infty$ and $\tau_j$, respectively, are the flow temperature change and the time step from the recorder output of the jet flow temperature history. In the present work, the jet flow temperature $T_\infty$ is determined by the thermocouple measurement in the pressure chamber prior to jet issue. The variation of $T_\infty$ with time is recorded and approximated by step changes. With the color change time $t$ at any location, the resulting superposed solution, Eq. (3), is used to solve for the local heat transfer coefficients on the target surface.

## 4. Results and discussion

For jet array impingement heat transfer over a plate with film holes, the geometric/thermo-fluid parameters, e.g., geometry of jet orifices, Reynolds number, cross-flow, jet-to-target spacing, and their coupling effects have a considerable impact on the characteristics of the fluid flow and heat transfer. The heat transfer performance is characterized by Nusselt number distributions. In this work, the emphasis is focused on the effects of jet-to-target spacing, the arrangement of film holes, and orifice aspect ratio under different jet Reynolds numbers. A typical case is considered as $Re = 3000$, jet-to-plate spacing $Z = 3$ and jet aspect ratio AR = 0.5.

Figs. 4–6 show the effects of Reynolds number on the local Nusselt number distribution with AR = 0.5 and $Z = 3.0$ for side-type, middle-type, and staggered-type target plates, respectively. The

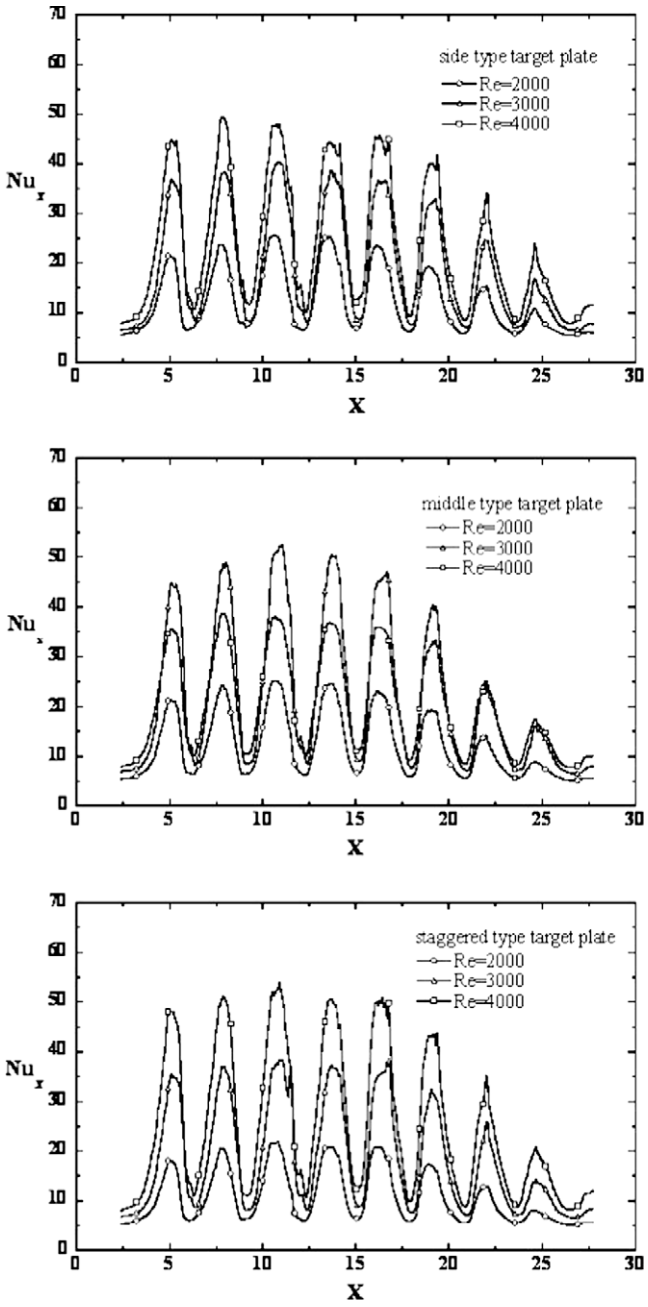


**Fig. 7.** The effects of Reynolds number on the longitudinal ($X$ direction) variation of the spanwise average of Nusselt number with AR = 0.5 and $Z$ = 3 for three types of target plates.

areas with red color and blue color indicate the portions of high and low local Nusselt number. Each red spot appears at the area under the corresponding jet orifice. It is clear that local $Nu$ is significantly increased with increasing $Re$ for all types of arrangements since the impinging force on the target plate is raised. More heat transfer is shown by larger red areas. It is noted in these three figures that the red spots shift with different extents. This is due to the cross-flow which shifts the heat transfer peaks toward the two exits of the flow channel. It can be seen that the red spots in the center region are larger and less shifted than those closed to the exits. The cross-flow develops along the channel direction. It causes more apparent peak shift and reduces the local heat transfer near the exits. The distortion of the red spots also indicates the existence of the cross-flow. The asymmetry of the figures indicates that the cross-flow is not even on the two ends because the jets come from left side of the pressure chamber. It is easier for the air to form cross-flow in co-direction than in counter-direction. In addition, it is also observed that there exist red spots in some of the film hole areas. The flow through the orifices creates circulation at the downstream of the film holes on the target plate and results in a secondary heat transfer. At high $Re$, some of the red spots under jet orifices and those at film holes grow to cluster together. This means that the coupling effects of Reynolds number and film hole enhances the heat transfer in the surrounding regions under the corresponding orifices. Considering this influence, it is seen that at high $Re$, the target plates of middle-type and staggered-type present a better heat transfer since the red spot clusters are larger.

**Table 1**
Averaged Nusselt number $\overline{Nu}$ for different $Re$ at AR = 0.5 and $Z$ = 3.

| $Re$ | Type | | |
|---|---|---|---|
| | Side | Middle | Staggered |
| 2000 | 12.186 | 11.942 | 10.700 |
| 3000 | 18.523 | 21.832 | 18.311 |
| 4000 | 23.603 | 23.293 | 25.175 |

The effects of Reynolds number on the longitudinal ($X$ direction) variation of the spanwise average of $Nu$ at AR = 0.5 and $Z$ = 3 for three types of target plates are shown in Fig. 7. The averaged $Nu$ is raised with increasing $Re$ for all types of film hole arrangement. All the curves present almost the same local minimum values, but not the same maximum ones. This indicates that heat transfer enhancement is constrained in the near by regions of the jet orifices. It is interesting to see that the staggered-type target plate gives rise to the most significant heat transfer at $Re$ = 4000, while it results in the lowest heat transfer at low $Re$. The middle-type target plate presents the best averaged $Nu$ for $Re$ = 3000 and the side-type target plate is the most effective for $Re$ = 2000. The values of $Nu$ are summarized in Table 1 and show this trend. It is also observed that the averaged $Nu$ for staggered-type target plate is low at low $Re$ and is drastically increased with increasing $Re$. In addition, the averaged $Nu$ for side-type target plate is the highest at low $Re$, but grows slowly with increasing $Re$. This leads to the speculation that the optimal design of heat transfer depends on the Reynolds number as well as the arrangement of film holes.

The effect of jet-to-target spacing $Z$ on the Nusselt number distribution at AR = 0.5 and $Re$ = 3000 for side-type, middle-type, and staggered-type target plates, are presented in Figs. 8–10, respectively. It is clear that $Nu$ increased with decreasing $Z$ value. All these three types of target plates present enhancement in heat transfer (by larger red spots) at small $Z$. This is due to the stronger shear force resulted from stronger impingement. Smaller jet-to-target spacing also gives rise to stronger cross-flow and by turn results in more significant heat transfer peak shift and red spot distortion on the plates. Although stronger cross-flow exists with smaller $Z$, the increased impingement overcomes the effect and results in better heat transfer. Comparison of the figures reveals that the middle-type target plate presents the best heat transfer at smaller spacing ($Z$ = 1.5, 3.0) but the worst at larger spacing ($Z$ = 4.5). The middle-type arrangement helps clustering the adjacent red spots under the jet orifices and show larger red areas. It can be explained that the middle arrangement results in more suitable thermal flow field for smaller jet-to-target spacing. It is also noticed in these figures that the heat transfer peaks are shifted toward to the two ends for smaller $Z$ and are shifted toward to the right end for greater $Z$. This indicates that the cross-flow causes shift of jets toward the two exits in the thinner impingement chamber. While in the thicker chamber, inertia of flow through

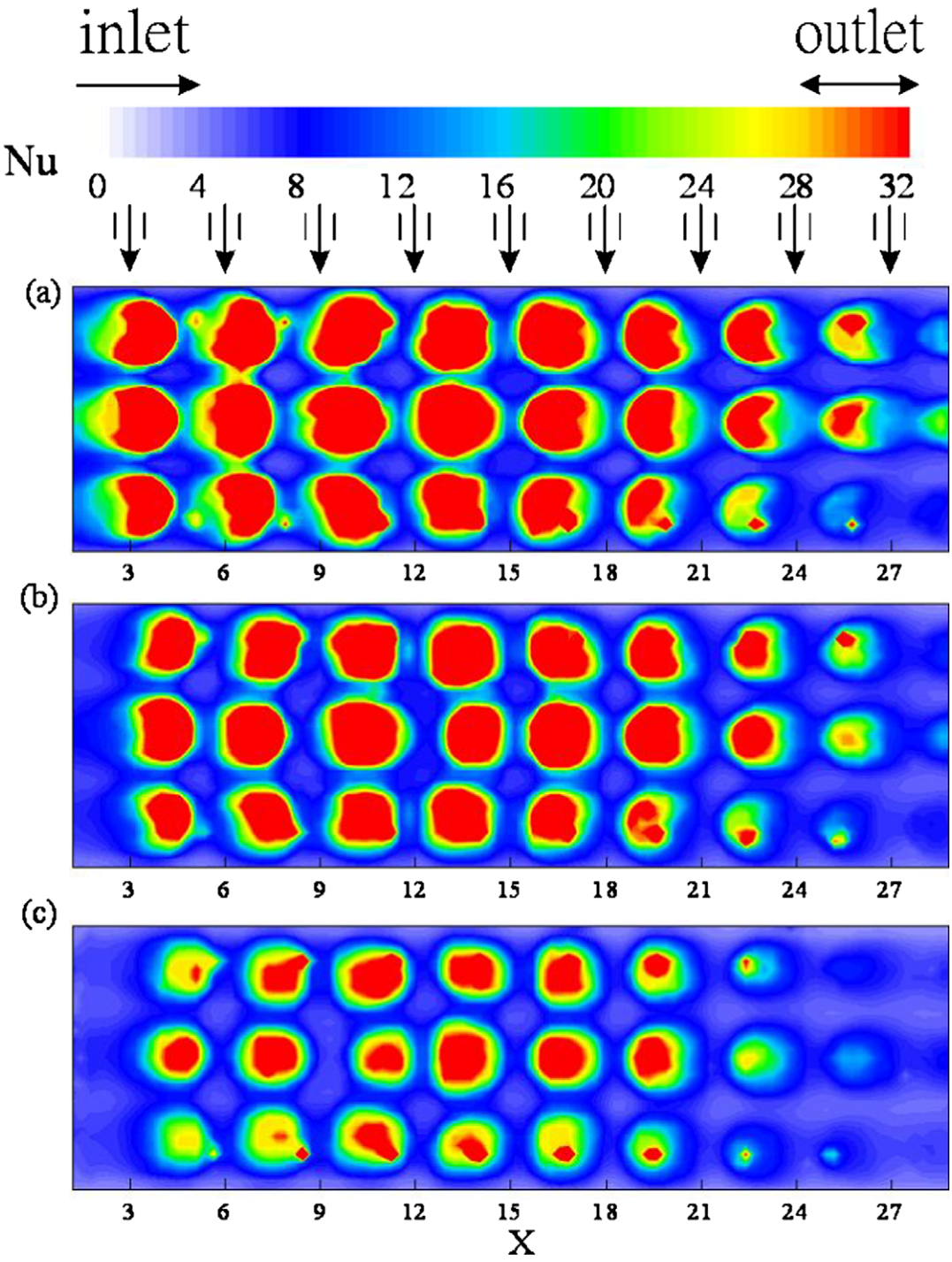


**Fig. 8.** The effect of jet-to-target spacing $Z$ on the Nusselt number distribution with AR = 0.5 and $Re$ = 3000 for side-type target plate at $Z$= (a) 1.5; (b) 3.0; and (c) 4.5.

the orifices influences the main stream and causes the shift toward the right exit.

Fig. 11 shows the effect of jet-to-target spacing on the longitudinal ($X$ direction) variation of the spanwise average of $Nu$ at AR = 0.5 and $Re$ = 3000 for three types of target plates. Similar to Fig. 7, the curves in Fig. 11 show almost the same local minimum averaged $Nu$, but disparate maximum values. Again similar to the trend in Fig. 7, the effects are also found restricted in the surrounding areas of the jets. The target plate with middle-type target plate at $Z$ = 3 and 1.5 presents heat transfer maximal higher than the other two. It indicates that this arrangement of target plate is better for low jet-to-target spacing due to coupling enhancement. Comparison for the curves of the other two arrangements shows slight differences. It means the coupling effect is not apparent for these arrangements. Fig. 12 depicts comparison of the longitudinal ($X$ direction) spanwise average of Nusselt number for different target plates at AR = 0.5, $Z$ = 3.0, and $Re$ = 3000. It is clear that all target plates with film hole result in higher $Nu$ value than the smooth one. Among them, the plate of middle-type performs most effectively. This phenomenon is even more apparent when $Z$ is reduced.

The effect of the jet geometry, orifice aspect ratio, on the heat transfer distribution for middle-type target plate at $Re$ = 3000 is shown in Fig. 13. It is found in Fig. 13(a)–(c) that heat transfer per-

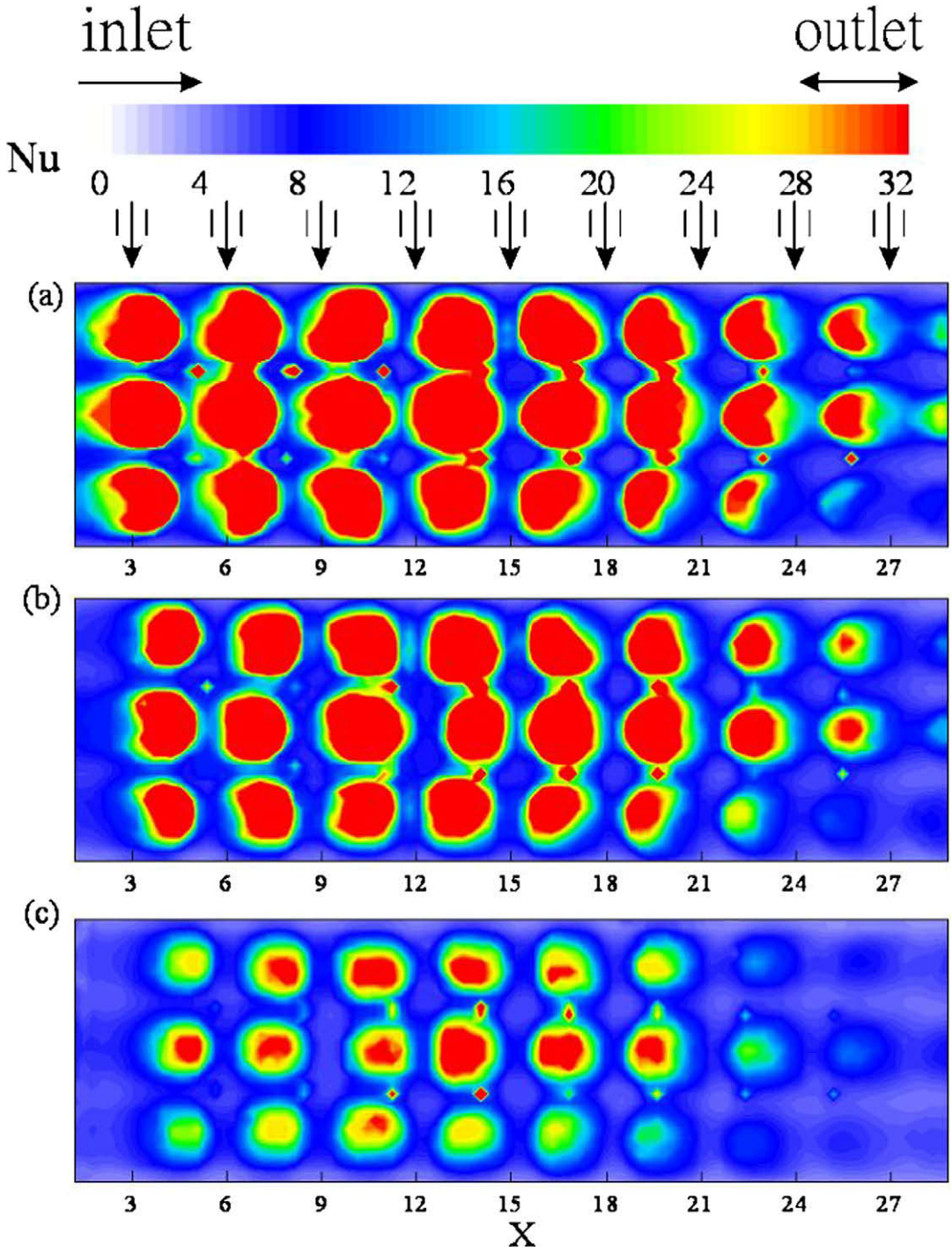


**Fig. 9.** The effect of jet-to-target spacing $Z$ on the Nusselt number distribution with AR = 0.5 and $Re$ = 3000 for middle-type target plate at $Z$= (a) 1.5; (b) 3.0; and (c) 4.5.

formance apparently decreases with increased AR when AR is large ($\geqslant$1.0). This is due to the non-uniform flow field and inclined flow in the impingement chamber. Larger AR means narrower impinging flow, which results in impinging locations (red spots) shifted toward the right exit. This phenomenon arises mainly from the effect of inertia momentum. The air flow from orifices of major axis parallel to main stream tends to incline toward right in the impingement plate. It by turn reduces the impinging force on the target plate. Thus the heat transfer peaks are smaller and are shifted toward the right side exit ($X$ = 30). On the other hand, the cross-flow in the impingement chamber is more influential than the inertia effect for smaller AR. The effects of cross-flow tend to sweep the jets toward both exits. An AR less than 1 means the long axis of the jets is vertical to the main flow direction of air. It is easy to see that orifices of AR = 0.5 presents better performance than those of AR = 0.25. According to [28], a smaller AR value results in stronger effects of cross-flow and less inertia effects. Although the images show almost no difference between AR = 1.0 and AR = 0.5, it can be found in Table 2 that the averaged Nusselt number $\overline{Nu}$ of the jet with AR = 1.0 results in the highest value. Over all comparisons indicate that both axial inertia and cross-flow suppress the heat transfer. Among them, circular jet shows the ulti-

mate composed result. It is also noted in Table 2 that the averaged $\overline{Nu}$ for AR = 0.5 and AR = 0.25 are higher than those for AR = 2.0 and AR = 4.0, respectively. Besides, Fig. 13(d) and (e) present heat transfer peak shift slighter than Fig. 13(b) and (c). That means an elliptic orifice of major axis vertical to $X$ direction results in less heat transfer than that of major axis along $X$ direction.

## 5. Conclusions

The experimental results for the range of parameters, $2000 \leq Re \leq 4000,\ 1.5 \leq Z \leq 4.5,\ 0.25 \leq AR \leq 4$, with different arrangement of film holes on the target plate have been investigated. Based on the experimental result, the major conclusions of the work can be drawn as the following:

1. Jets with higher Reynolds number cause more effective heat transfer since the higher velocity buffs cross-flow effect. The target plate with staggered-type arrangement is most effective for high $Re$ (4000) while latest effective for low $Re$ (2000). On the other hand, the target plate with side-type is not good for high $Re$, but the best for low $Re$. Besides, the jets of $Re$ = 3000 enhances the plate with middle-type the most. The performance of the system depends on the arrangement of film holes as well as the flow

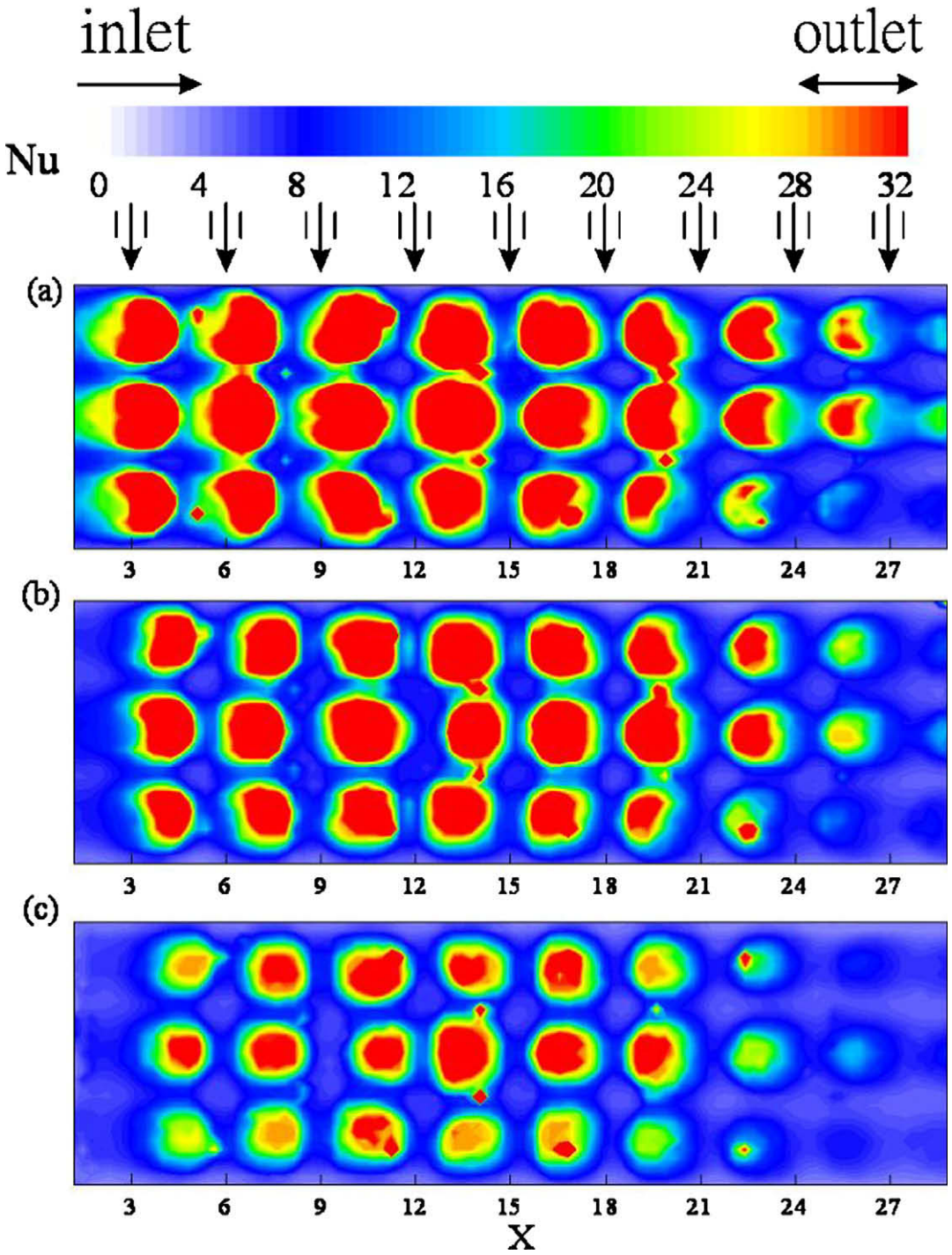


**Fig. 10.** The effect of jet-to-target spacing $Z$ on the Nusselt number distribution with AR = 0.5 and $Re$ = 3000 for staggered-type target plate at $Z$= (a) 1.5; (b) 3.0; and (c) 4.5.

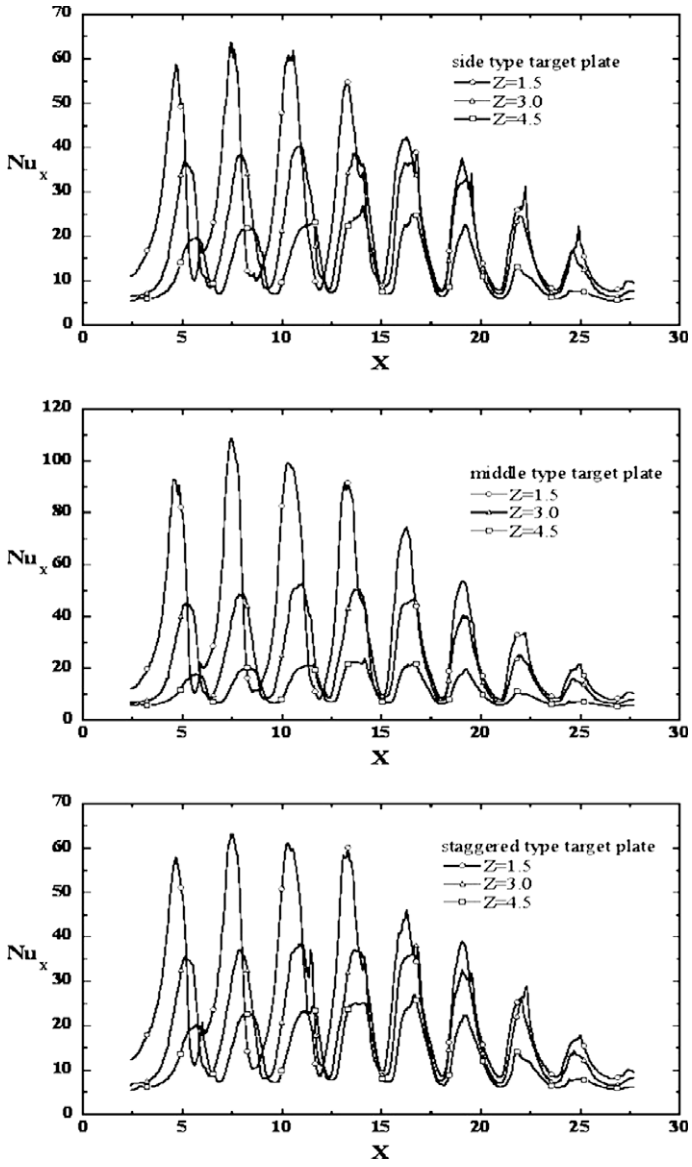


**Fig. 11.** The effects of jet-to-target spacing on the longitudinal (*X* direction) variation of the spanwise average of Nusselt number with AR = 0.5 and *Re* = 3000 for three types of target plates.

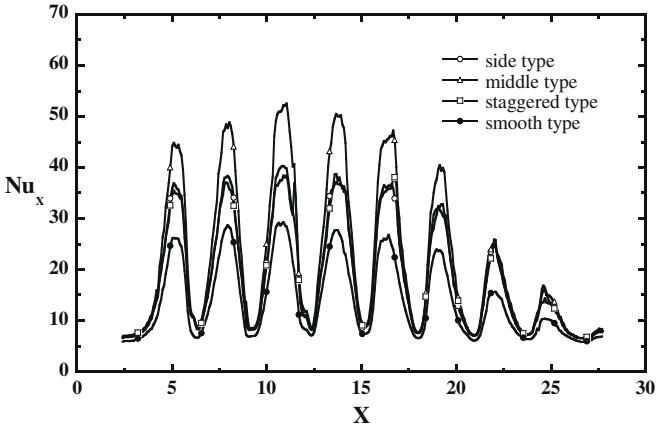


**Fig. 12.** The longitudinal (*X* direction) spanwise average of Nusselt number at AR = 0.5, *Z* = 3.0, and *Re* = 3000 for various target plates.

rate. The longitudinal (*X* direction) variation of the spanwise average of Nusselt number shows that the heat transfer enhancement is restricted in the regions surrounding the jet.

2. Lowering the impinging spacing increases both impinging force and cross-flow. But the increment of impinging force is more significant than that of cross-flow. This by turn raises the total heat transfer. The enhancement on the middle-type target plate is more significant than those on the other two types of target plates.
3. When a middle-type target plate is considered, the experimental results show that the aspect of 1.0 (circular orifice) causes more uniform heat spray, stronger jet impingement, and the most significant heat transfer. Contrarily, narrower jets result in less heat transfer due to stronger cross-flow or more significant axial inertia momentum.
4. The results also indicate that for the same shape, an orifice of major axis vertical to main stream direction performs better than that of along main stream direction.

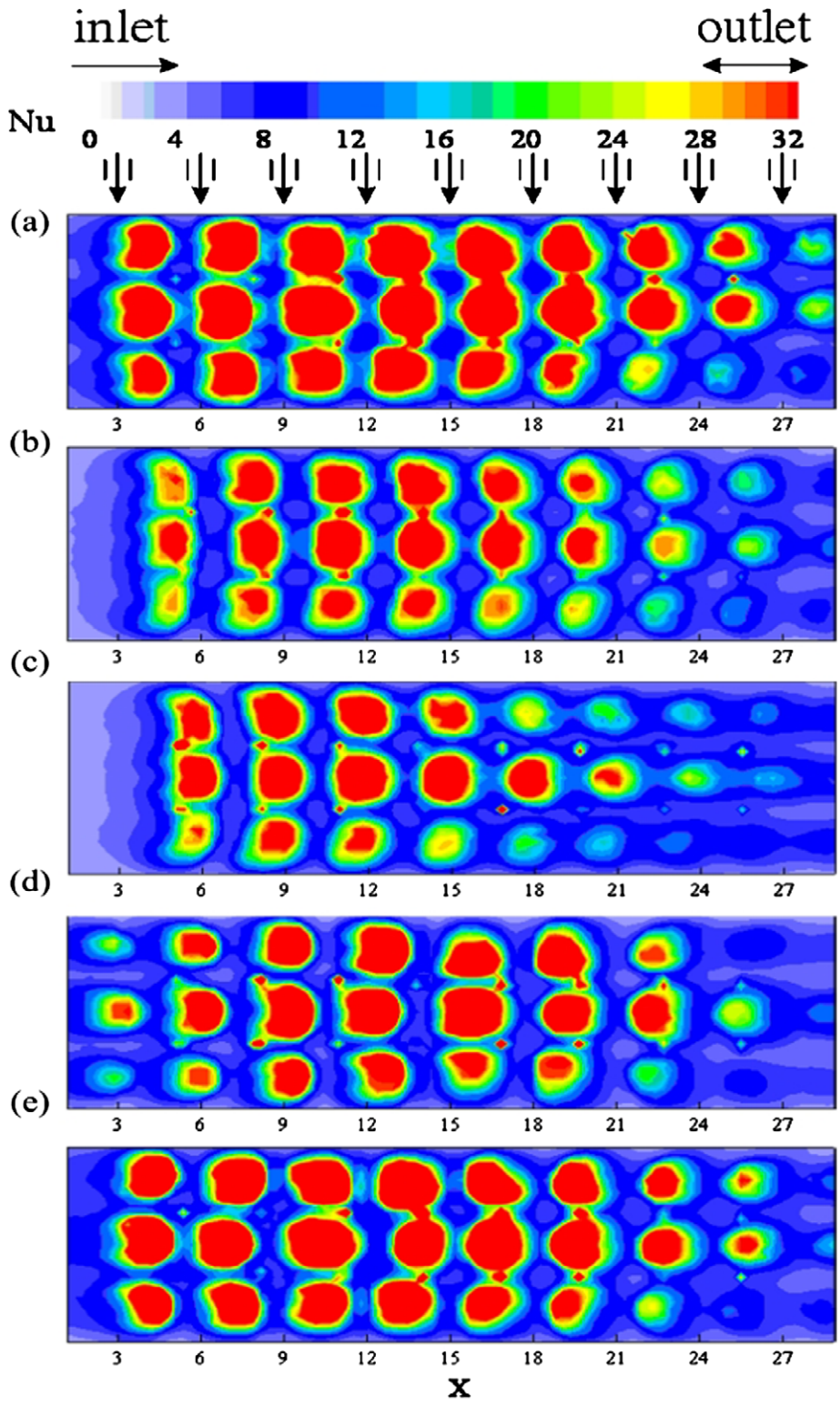


**Fig. 13.** The effects of the jet geometry on the heat transfer distribution for middle-type target plate at $Re = 3000$ for AR= (a) 1; (b) 2; (c) 4; (d) 0.25; and (e) 0.5.

**Table 2**
Averaged Nusselt number $\overline{Nu}$ for different aspect ratio AR, at $Z = 3$, $Re = 3000$ with middle-type film hole.

| AR | 0.25 | 0.5 | 1 | 2 | 4 |
|---|---|---|---|---|---|
| $\overline{Nu}$ | 16.096 | 21.832 | 23.672 | 15.096 | 13.786 |

## Acknowledgement

The financial support of this study by the National Science Council of Taiwan, ROC, through the Grant No. NSC 96-2212-E211-011, is gratefully acknowledged.

## References


[1] R. Viskanta, Heat transfer to impinging isothermal gas and flame jets, Exp. Therm. Fluid Sci. 6 (1993) 111–134.

[2] K. Jambunathan, E. Lai, M.A. Moss, B. Button, A review of heat transfer data for single circular jet impingement, Int. J. Heat Fluid Flow 13 (1992) 106–115.

[3] N.T. Obot, A.S. Majumdar, W.J.M. Douglas, The effect of nozzle geometry on impingement heat transfer under a round turbulent jet, ASME Paper No. 79-WA/HT-53, ASME, 1979.

[4] K. Kataoka, Impingement heat transfer augmentation due to large scale eddies, in: Proceedings of the Ninth International Heat Transfer Conference, vol. 1, Washington, DC, 1990, pp. 255–273.

[5] C.K.W. Tam, T.D. Norum, Impingement tones of large aspect ratio subsonic rectangular jets, AIAA J. 30 (1992) 304–311.

[6] F. Hussain, H.S. Husain, Elliptic jets. Part 1. Characteristics of unexcited and excited jets, J. Fluid Mech. 208 (1989) 257–320.

[7] H.S. Husain, F. Hussain, Elliptic jets. Part 2. Dynamics of coherent structures: pairing, J. Fluid Mech. 233 (1991) 439–482.

[8] H.S. Husain, F. Hussain, Elliptic jets. Part 3. Dynamics of preferred mode coherent structure, J. Fluid Mech. 248 (1993) 315–361.

[9] C.M. Ho, E. Gutmark, Vortex induction and mass entrainment in a small-aspect-ratio elliptic jet, J. Fluid Mech. 179 (1987) 383–405.

[10] S.J. Lee, J. Lee, D. Lee, Local heat transfer measurements from an elliptic jet impinging on a flat plate using liquid crystal, Int. J. Heat Mass Transfer 37 (1994) 967–976.

[11] J. Lee, S.J. Lee, The effect of nozzle aspect ratio on stagnation region heat transfer characteristics of elliptic impinging jet, Int. J. Heat Mass Transfer 43 (2000) 555–575.

[12] A.M. Huber, R. Viskanta, Effects of jet–jet spacing on convective heat transfer to confined, impinging arrays of axisymmetric air jets, Int. J. Heat Mass Transfer 37 (1994) 2859–2869.

[13] L.W. Florschuetz, C.P. Truman, D.E. Metzger, Streamwise flow and heat transfer distribution for jet impingement with crossflow, ASME J. Heat Transfer 103 (1981) 337–342.

[14] N.T. Obot, T.A. Trabold, Impingement heat transfer within arrays of circular jets. Part 1: effects of minimum, intermediate, and complete crossflow for small and large spacings, J. Heat Transfer 109 (1987) 872–879.

[15] C. Gau, C.C. Lee, Impingement cooling flow structure and heat transfer along rib-roughened walls, Int. J. Heat Mass Transfer 35 (1992) 3000–3020.

[16] W.M. Yan, H.C. Liu, C.Y. Soong, W.J. Yang, Experimental study of impinging heat transfer along rib-roughened walls by using transient liquid crystal technique, Int. J. Heat Mass Transfer 48 (2005) 2420–2428.

[17] V. Treuren, K.W. Wang, Z. Ireland, T.V. Jones, Detailed measurements of local heat transfer coefficient and adiabatic wall temperature beneath an array of impingement jets, ASME J. Turbomachinery 116 (1994) 369–374.

[18] D.H. Rhee, P.H. Yoon, H.H. Cho, Local heat/mass transfer and flow characteristics of array impinging jets with effusion holes ejecting spent air, Int. J. Heat Mass Transfer 46 (2003) 1049–1061.

[19] K. Kanokjaruvijit, R.F. Martinez-botas, Jet impingement on a dimpled surface with different cross schemes, Int. J. Heat Mass Transfer 48 (2005) 161–170.

[20] G.S. Azad, Y. Huang, J.C. Han, Impingement heat transfer on dimpled surfaces using a transient liquid crystal technique, AIAA J. Thermophys. Heat Transfer 14 (2000) 186–193.

[21] Y. Huang, S.V. Ekkad, J.C. Han, Detailed heat transfer distributions under an array of orthogonal impinging jets, AIAA J. Thermophys. Heat Transfer 12 (1998) 73–79.

[22] G. Wagner, M. Kotulla, P. Ott, B. Weigand, J. von Wolfersdorf, The transient liquid crystal technique: influence of surface curvature and finite wall thickness, ASME Paper GT2004-53553, 2004.

[23] J.C. Han, Heat transfer and friction characteristics in rectangular channels with rib turbulators, ASME J. Heat Transfer 110 (1988) 321–328.

[24] Y.J. Hong, S.-S. Hsieh, Heat transfer and friction factor measurements in ducts with staggered and in-line ribs, ASME J. Heat Transfer 115 (1993) 28–65.

[25] W.M. Yan, R.C. Hsieh, C.Y. Soong, Experimental study of surface-mounted obstacle effects on heat transfer enhancement by using transient liquid crystal thermography, ASME J. Heat Transfer 124 (2002) 762–769.

[26] C. Gau, C.M. Chung, Surface curvature effect on slot-air-jet impingement cooling flow and heat transfer process, ASME J. Heat Transfer 113 (1991) 858–864.

[27] J.M. Miao, C.Y. Wu, Numerical approach to hole shape effect on film cooling effectiveness over flat plate including internal impingement cooling chamber, Int. J. Heat Mass Transfer 49 (2006) 919–938.

[28] R.J. Goldstein, J.F. Timmer, Visualization of heat transfer from arrays of impinging jets, Int. J. Heat Mass Transfer 25 (1982) 1857–1868.

[29] J.W. Baughn, S. Shimizu, Heat transfer measurement from a surface with uniform heat flux and an impinging jet, ASME J. Heat Transfer 111 (1989) 1096–1098.

[30] W.M. Yan, H.S. Mei, H.C. Liu, C.Y. Soong, W.J. Yang, Measurement of detailed heat transfer on a surface under arrays of impinging elliptic jets by a transient liquid crystal technique, Int. J. Heat Mass Transfer 47 (2004) 5235–5245.

[31] D. Priedeman, V. Challahan, B.W. Webb, Enhanced of liquid jet impingement heat transfer with surface modification, ASME J. Heat Transfer 116 (1994) 486–489.

[32] M.K. Chyu, H. Ding, J.P. Downs, A. Van Sutendael, F.O. Soechting, Determination of local heart transfer coefficient based on bulk mean temperature using a transient liquid technique, ASME Paper No. 97-GT-489, 1997.

[33] J.-J. Hwang, C.-S. Cheng, Impingement cooling in triangular ducts using an array of side-entry wall jets, Int. J. Heat Mass Transfer 44 (2001) 1053–1063.